JACS
JOURNAL OF THE AMERICAN CHEMICAL SOCIETY
pubs.acs.org/JACS
Article

Single-Atom Migration into a Chiral Multilayer Nanocluster Architecture

Yuhao Jin, Hao Fang, Haoyu Pan, Zhenyi Zhang, Chaofeng Liu, Long Yang,* Zheng Zhou,* and Haixiang Han*

Cite This: https://doi.org/10.1021/jacs.6c03831
Read Online

ABSTRACT: Colloidal nanocrystals are generally regarded as rigid solid entities, rarely exhibiting the structural adaptability observed in molecular cages, such as fullerenes, which can undergo carbon framework reduction and encapsulate guest cations without structural reorganization. Here, by creating two enantiomeric pairs of high-nuclearity copper sulfide nanoclusters with a mixed-valence Cu(II)/Cu(I) configuration, we endow these nanoscale assemblies with an intrinsic capacity for electron uptake under mild reducing conditions. The resulting charge imbalance provides an effective thermodynamic driving force that realizes a positively charged metal ion migrating inward through multiple atomic layers and occupying the cluster core. This system thus represents a rare example of a nanocluster platform that simultaneously combines reduction tolerance and structural robustness, preserving its atomic framework despite the incorporation of a single atom effectively modifying the electronic structure, particularly the local chirality. In situ absorption and circular dichroism spectroscopies establish that the transformation proceeds through a continuous, single-particle process rather than a fragmentation-reconstruction pathway, while ex situ pair distribution function analysis resolves key local steps in the structural evolution, offering mechanistic insights into this unique migration behavior.

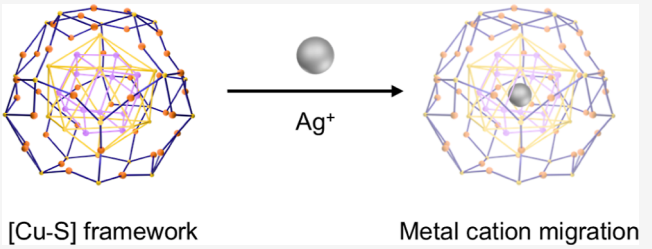

INTRODUCTION

The migration of a single atom into the innermost site of a nanoscale host—in a manner that leaves the host structure essentially intact—is a profoundly counterintuitive phenomenon. It challenges long-held paradigms in nanoscience and demands a clear rationalization of the apparent conflict between atomic mobility and structural rigidity at the nanometer scale.[1−5] A central question would be what is the driving force that enables such unidirectional motion? When materials are reduced to the nanoscale regime, surface atoms (which typically possess elevated energy and enhanced reactivity) comprise a large fraction of the total atomic population. These surface atoms are more accessible for interactions with guest ions, whereas interior atoms are more inert and spatially isolated, thereby suppressing inward movement.[6,7] As a consequence, guest−host interactions in nanocrystals are typically manifested as surface ion-exchange processes that modulate the outer atomic arrangement—an approach widely employed to tune surface composition and reactivity, yet one that rarely induces rearrangement within the interior lattice.[8,9] When single-atom migration does occur, the inserted atom necessarily occupies an otherwise vacant or non-native lattice site along its dynamically shuttling pathway.[1,10−12] This occupation introduces local lattice strain and coordination bias, creating an intrinsic mismatch between the incoming atom and its surrounding framework. Under conventional understanding, such lattice distortion would be expected to hinder further atom motion and trigger structural reconstruction, or even fragmentation of the nanocrystal once the strain exceeds a critical threshold, making the preservation of the host structure extremely difficult.[2,13,14] Another critical consideration concerns the charge state of the guest species. If the guest atom exists as a charged ion rather than a neutral atom, charge neutrality must be preserved through the concurrent participation of counterions or charge redistribution within the host lattice. In other words, what may appear to be a simple atomic migration process intrinsically entails a complex electrostatic adjustment, in which compensating species must accompany the migrating ion to maintain overall neutrality. This coupling between ionic motion and charge compensation introduces an additional layer of structural and electronic complexity, potentially influencing local bonding configurations and even the global structural characteristics of the host framework.[2,15−21]

Received: February 19, 2026
Revised: May 7, 2026
Accepted: June 15, 2026

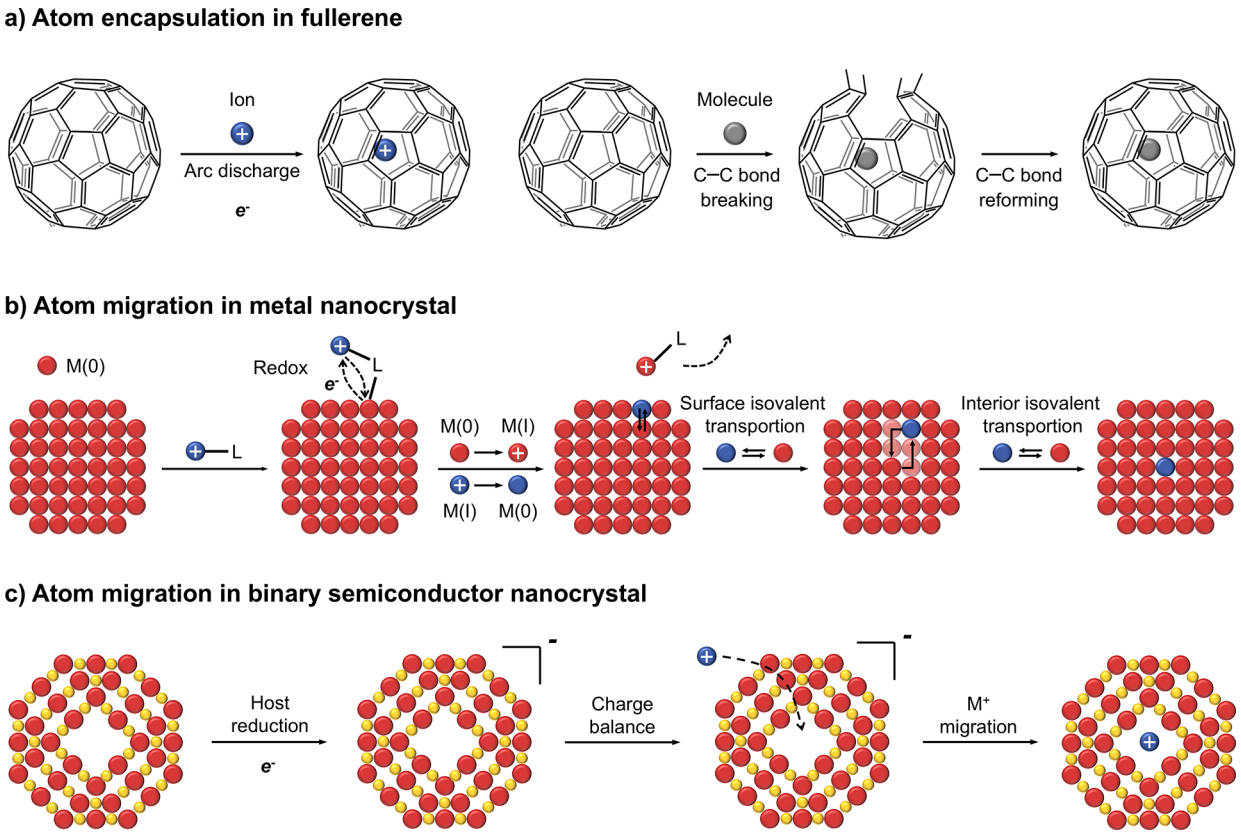

Figure 1. Schematic illustration of single atom migration within different nanoscale frameworks. (a) Atom encapsulation in fullerene. (b) Atom migration in metal nanocrystal. (c) Atom migration in a binary semiconductor crystal (this work).

The term single-atom migration is often misconceived as synonymous with central atom doping. In fact, central atom doping is a more general conception also referring to a synthetic incorporation process, in which a heteroatom is trapped at the center during the early stages of crystal growth.[3,18,20,21] In contrast, single-atom migration especially denotes a postsynthetic insertion event, wherein an atom directly goes into the preformed host framework—a phenomenon that is far rarer and mechanistically more intriguing.[10,22,23] Single-atom migration provides insight into the structural adaptability of nanomaterials, demonstrating that rigid hosts can undergo local atomic reconfiguration without collapse. This phenomenon broadens the functional landscape of nanocrystals, enabling tunable electronic, optical, and catalytic properties beyond their native limits.[10,17,19]

To date, several distinct systems have been established for the investigation of single-atom migration within nanoscale frameworks, spanning molecular-scale fullerenes to extended inorganic nanocrystals. Among them, endohedral fullerenes and their derivatives represent archetypal, atomically precise nanocages capable of encapsulating guest species while preserving their robust, spherical carbon network. High-energy techniques such as arc discharge can transiently open the cage, permitting atomic or molecular insertion, whereas soft-chemistry routes achieve controlled encapsulation through regioselective functionalization that creates local entry sites under milder conditions (Figure 1a).[23−28] These strategies have successfully progressed atomic-level studies of single-cation inclusion (e.g., $Li^+@C_{60}^-$, $La^{3+}@C_{82}^{3-}$), multimetal bonding (e.g., $Sc_2@C_{82}$, $Y_2@C_{82}$), and molecular confinement (e.g., $H_2@C_{60}$, $H_2O@C_{60}$).[23−29]

Extending this concept to classical metal or semiconductor nanocrystals presents greater complexity. In such systems, single-atom migration often requires the cooperative action of multiple driving forces—such as lattice strain, redox potential, and surface energy gradients—and remains challenging to control.[1,4,10−12,30−35] As a result, heteroatomic alloying is more commonly observed than discrete atomic relocation. Moreover, unlike fullerenes, colloidal nanocrystals have rarely exhibited the redox flexibility required to gain or lose electrons without structural disruption. This is probably due to the fact that the inorganic framework in nanocrystals lacks the capability to delocalize additional electrons like sp^2-hybrid carbons.[36] Thus, most inorganic hosts cannot easily undergo redox adjustment to accommodate ionic species, necessitating charge compensation through counterions or ligand reorganization, which can inadvertently change the host lattice.[2,37,38] Nevertheless, several notable examples of metal clusters have demonstrated that atomic migration within a nanocrystal is feasible with distinct pathways, where heteroatoms typically migrate isovalently (e.g., Au(0) → Ag(0)) toward the core (see more examples summarized in Supporting Information, Table S8) (Figure 1b).[11,30−35]

Here, we demonstrate for the first time that a binary copper sulfide nanocluster system with a mixed-valence Cu(II)/Cu(I) configuration exhibits fullerene-like redox resilience, enabling reduction without structural degradation. Uniquely, the host framework itself can be reduced to accommodate and delocalize an extra electron while preserving its atomic integrity, creating an intrinsic charge imbalance that pumps a guest Ag^+ cation into the cluster's geometric center (Figure 1c). Moreover, this nano system also demonstrates structural

https://doi.org/10.1021/jacs.6c03831
J. Am. Chem. Soc. XXXX, XXX, XXX−XXX

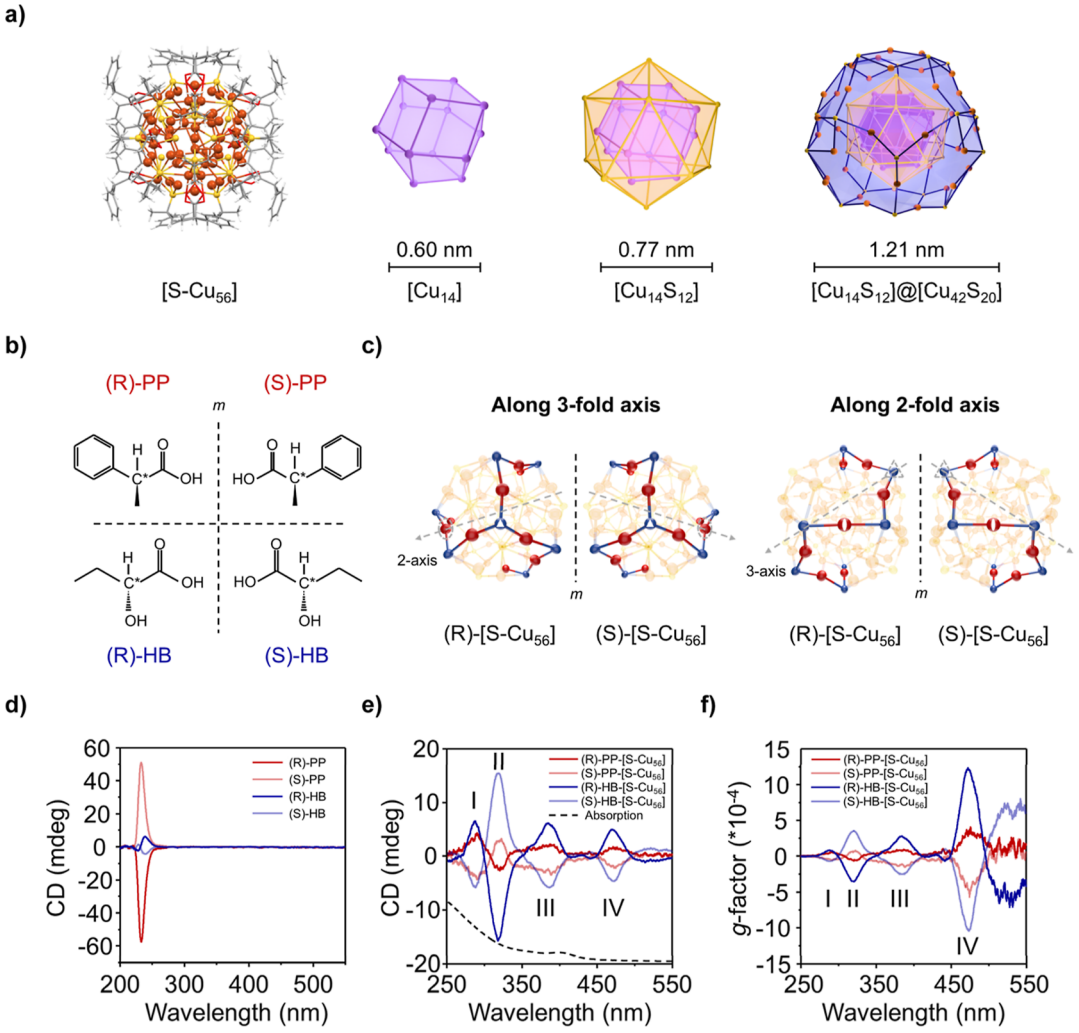

Figure 2. (a) Multishell structure of the parent chiral cluster (*R*)-PP-[S−Cu_{56}]. (b) Chiral carboxylic acid employed in the synthesis of chiral copper sulfide nanoclusters. (c) Chiral features of the as-prepared parent PP-[S−Cu_{56}] clusters viewed along the 3-fold axis and 2-fold axis. (d) CD spectra of pure (*R*/*S*)-PP and (*R*/*S*)-HB ligands dissolved in DCM, measured at a concentration of 0.3 mg/mL. (e) CD spectra of PP-[S−Cu_{56}] and HB-[S−Cu_{56}] dissolved in DCM, measured at a concentration of 0.2 mg/mL. (f) Calculated *g*-factor plots based on figure e.

robustness, allowing for chirality to be introduced by employing targeting chiral ligands, which not only enables the successful synthesis of chiral metal sulfide nanomaterials but also provides a versatile chiral toolbox to probe migration dynamics and explore how central-atom incorporation influences chiroptical properties within a rigid, integrated nanostructure.

RESULTS AND DISCUSSION

Synthesis of Parent Chiral Nanoclusters

As the first step, we have prepared two new enantiomeric pairs of copper sulfide nanoclusters, (*R*)/(*S*)-PP-[S−Cu_{56}] and (*R*)/(*S*)-HB-[S−Cu_{56}] (hereafter, [S−Cu_{56}] is used as a general designation for all four parent clusters. PP-[S−Cu_{56}] and HB-[S−Cu_{56}] denote the two enantiomeric pairs distinguished by their respective chiral ligands, with chirality specified using (*R*)/(*S*) descriptors) as the parent nano architectures using the corresponding chiral carboxylate ligands ((*R*/*S*)-2-phenylpropionic acid ($PhCH(CH_3)COOH$, abbreviated as (*R*/*S*)-PP; (*R*/*S*)-2-hydroxybutanoic acid ($CH_3CH_2CH(OH)COOH$, abbreviated as (*R*/*S*)-HB))) (Figure 2b, see Supporting Information for more information). These clusters are structurally analogous, each exhibiting a distinct multishell architecture: an innermost rhombic dodecahedral [Cu_{14}] core, encapsulated by a [S_{12}] icosahedral shell, and further enclosed within an outer [$Cu_{42}S_{20}$] shell constructed from 12 edge-sharing, distorted five-pointed star units (Figures 2a and S8). With such a multishell structural configuration, the chirality originated from the surface ligands can be successfully transmitted into the inorganic [Cu−S] framework, thereby imparting intrinsic chirality to the nanocluster (Figures 2c and S8). The chiral features of these clusters can be conveniently recognized when viewed along their C_2- and C_3-rotational axes, with representative atoms highlighted (Figure 2c). Along the C_3 axis, the structure adopts a helical tripod-like arrangement, whereas along the C_2 axis, it appears as an up-and-down, dumbbell-like shape, both subjecting to their intrinsic symmetry elements. These chiral inorganic components afford distinct chiroptical responses, clearly differentiating them from the signals of the pure organic ligands (Figure 2d,e). In particular, while both neutral (*R*)/(*S*)-PP and (*R*)/(*S*)-HB ligands exhibit their characteristic circular dichroism (CD) features in the region below 260 nm (Figure 2d), the corresponding copper sulfide clusters display CD signatures

https://doi.org/10.1021/jacs.6c03831
J. Am. Chem. Soc. XXXX, XXX, XXX−XXX

spanning 265 to 500 nm (Figure 2e). Because of the close structural analogy of the inorganic framework, all four nanoclusters show similar CD profiles, each featuring four characteristic bands distributed across regions **I**−**IV** at around 290, 318, 385, and 470 nm, with a maximum at 290 nm for PP-[S−Cu_{56}] and 318 nm for HB-[S−Cu_{56}]. This spectral resemblance strongly indicates that the inorganic component, rather than the surfactant organic ligands in these intrinsically chiral nanocrystals, primarily governs the overall chiroptical response, which is likely mediated by electronic transitions within the inorganic framework or across the inorganic−organic interface. However, that does not mean to diminish the important role played by the organic ligands, but instead, it looks like the surfactant ligands have profound influence on the chiral strength reflected on the CD signals. Despite their similar profiles, the HB-[S−Cu_{56}] pair exhibits substantially stronger chiroptical intensities than the PP-[S−Cu_{56}] ones. The corresponding *g*-factor plots corroborate this trend, with HB-[S−Cu_{56}] exhibiting dissymmetry factors consistently about two times larger than those of PP-[S−Cu_{56}] across all absorption bands. Notably, the maximum *g* value for HB-[S−Cu_{56}] reaches approximately 1.2×10^{-3} (Figure 2f), which is rarely high among high-nuclearity cluster families, especially the Cu-based cluster system as they typically display low absorption extinction coefficient.[39−41] The enhancement underscores the roles of surface ligands playing in modulating chiroptical properties, potentially acting as chiroptical antennas that amplify the displaying chiral strength.[42−44] It is interesting to note that the CD spectra of the clusters deviate significantly from their absorption features, suggesting a considerable contribution from magnetic dipole-allowed transitions.[43,45,46]

Crucially, in contrast to typical metal clusters containing M(0)/M(I) species that are commonly prepared through a reduction route,[47,48] the current chiral [S−Cu_{56}] nanoclusters are obtained via an acid-assisted C−S bond cleavage strategy. This is a mildly oxidizing synthetic method that can yield copper in a mixed-valence of Cu(I)/Cu(II), even though the chemical formula alone would suggest a pure Cu(I) oxidation state.[39,49,50] Because simply calculating oxidation states from molecular formulas is often insufficient for correlating the actual chemophysical properties of nanoclusters, we instead adopt experimentally derived "displaying oxidation states" from X-ray photoelectron spectroscopy (XPS) and X-ray absorption near-edge structure (XANES) analyses (Supporting Information, Figures S4 and S6), which reflect the real electronic structure, as a more reliable basis for property prediction and correlation. Such an unusual feature later emerges as the key advantage to ultimately authorize occurrence of single-atom migration.

Directed Migration of a Guest Metal Cation into Chiral Nanoclusters

To achieve the migration of a metal cation into the center of the parent clusters, the copper sulfide framework must first undergo an appropriate degree of reduction. By virtue of the mixed-valence Cu(II)/Cu(I) configuration in clusters, it allows for the well-controlled electron uptake and the resulting charge imbalance, thereby providing an effective thermodynamic driving force that directs the guest metal cation to migrate into the cluster core. In this specific nanocluster system, strong reducing agents such as $NaBH_4$ immediately induce complete decomposition (Supporting Information Figure S2), which provides direct evidence of solidifying the oxidizing capability of the copper. After extensive screening, a mild organic thiolate is identified as the optimal choice because it functions not only as a gentle reducing agent but also as an X-type ligand capable of coordinating guest metal ions,[48,51] serving as an "all-in-one" solution that simultaneously facilitates controlled electron delivery and metal-ion transport. Building on this concept, AgS^tBu was employed as the precursor to investigate single-atom incorporation within the above four chiral copper sulfide nanoclusters (Figure 3a,b). The thiolate ligand is likely oxidized to form an RSSR disulfide dimer, which serves as a reducing reagent for the [S−Cu_{56}] framework, as suggested by ^{1}H NMR investigations (see the NMR section for more details). On the contrary, attempts to employ $AgNO_3$ or $AgBF_4$ as alternative silver sources failed to yield the desired products (Supporting Information, Figure S2), suggesting that reducing organic thiolate is essential for the ion transport process.

In a typical procedure, red crystalline [S−Cu_{56}] (Figure 3c) was mixed with AgS^tBu in DCM, yielding a yellowish solution at the very beginning (see Supporting Information for more information). As the reaction went on, the color of the solution slowly changed from yellow to dark brown within 60 min. After this, no further change was observed. The solution was then carefully transferred to an argon-filled glass tube, followed by layering CH_3CN onto the mother liquor. High-quality single crystals of Ag@[S−Cu_{56}] (the notation Ag@[S−Cu_{56}] follows the naming convention as the parent [S−Cu_{56}], indicating the incorporation of a single Ag atom at the center of the cluster assembly) can be obtained from solution in about 5 days. Quite different from the parent [S−Cu_{56}] cluster, the incorporation of Ag^+ dramatically changes the crystal color, from the original bright red to black (Figure 3c). The solid-state Ag@[S−Cu_{56}] is stable in the open air and soluble in DCM and toluene, while it has limited solubility in acetonitrile, hexane, and methanol.

Scanning electron microscopy (SEM) on single crystals of [S−Cu_{56}] and Ag@[S−Cu_{56}] reveals distinct morphologies (specifically (*R*)-PP-[S−Cu_{56}] and (*R*)-PP-Ag@[S−Cu_{56}] were selected here as representative examples, and were used throughout the following XPS, XANES and electrochemical investigations). The former demonstrates a rod-like shape, whereas the latter forms block-shaped crystals (Figure 3c), which suggests that they have different intermolecular interactions. Energy-dispersive X-ray spectroscopy (EDS) on Ag@[S−Cu_{56}] unambiguously confirmed the successful incorporation of Ag (Figure 3c), which is further verified through XPS (Figures 3d,e and S3). The XPS analysis additionally establishes the monovalent oxidation state for the Ag. Specifically, Ag@[S−Cu_{56}] features binding energies of Ag $3d_{3/2}$ and Ag $3d_{5/2}$ orbitals at 374.6 and 368.7 eV, which are comparable to the reference sample Ag(I)TFA (TFA = trifluoroacetate) and other reported Ag(I)-complexes and clusters, but obviously different from the metal Ag (Supporting Information, Figure S5).[47,48,52] Furthermore, the high-resolution Ag 3d spectra can be fitted using a single-component model for both spin−orbit components (Figure 3e), confirming that the central Ag^+ ions position a uniform chemical environment. XPS and XANES analyses on Cu unveil no discernible difference after Ag^+ insertion (Supporting Information, Figures S4 and S6). Thus, the additional electron introduced during the migration process is expected to be evenly delocalized over the entire [Cu−S] framework,[53,54] rendering any change in the oxidation state too subtle to be

https://doi.org/10.1021/jacs.6c03831
J. Am. Chem. Soc. XXXX, XXX, XXX−XXX

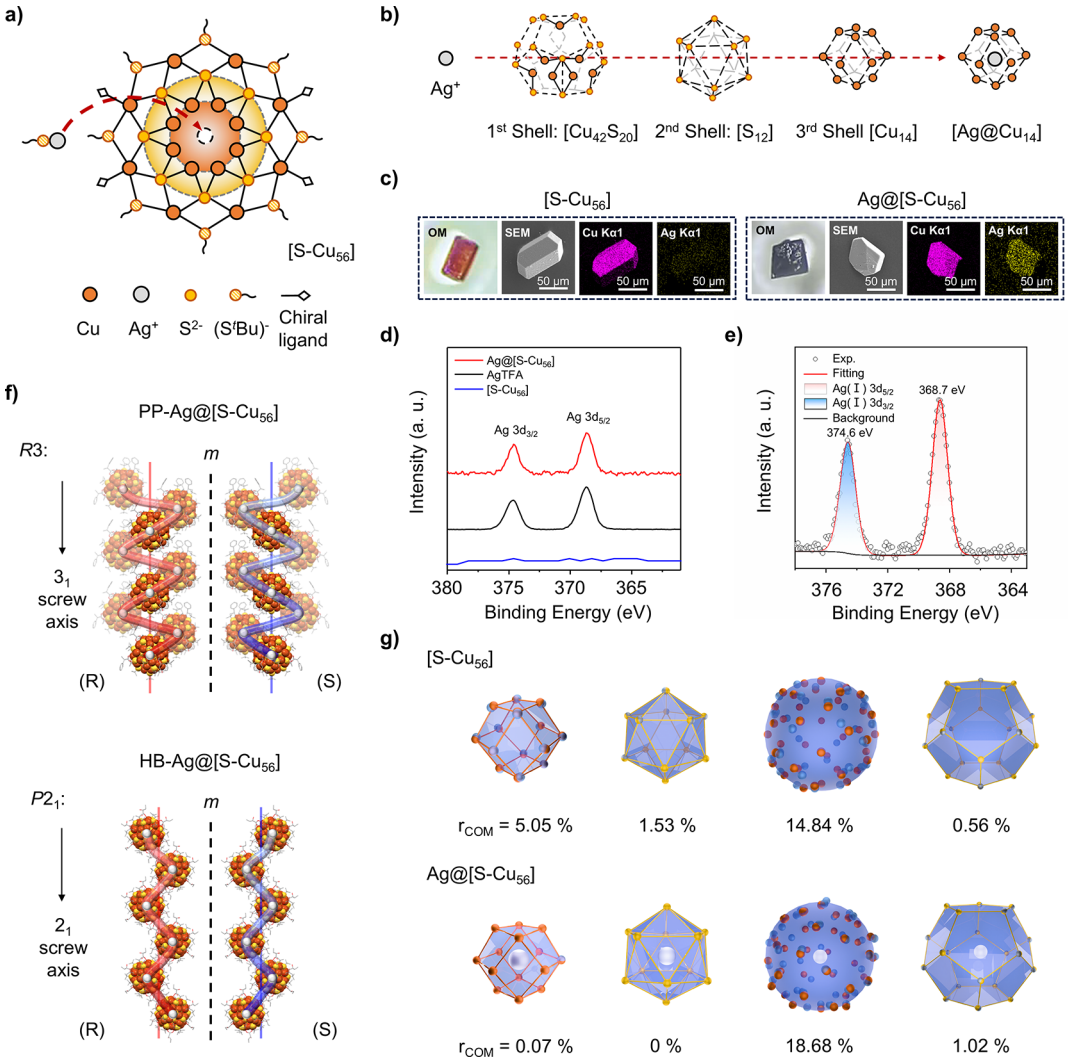

Figure 3. (a) Schematic illustration of the Ag^+ migration into the parent [S−Cu_{56}] nanocluster. (b) Schematic illustration of Ag atom incorporation into copper sulfide architecture by passing through its multishells. Solid lines indicate covalent bonds, and dashed lines represent relatively weak or absent interactions between atoms. (c) Optical microscopy, SEM images, and EDS element analysis of (*R*)-PP-[S−Cu_{56}] and (*R*)-PP-Ag@[S−Cu_{56}] single crystals. (d) Comparison of the high-resolution XPS spectra of the Ag 3d orbitals of (*R*)-PP-Ag@[S−Cu_{56}], AgTFA, and (*R*)-PP-[S−Cu_{56}]. (e) Experimental and simulated XPS spectra of Ag 3d orbitals for (*R*)-PP-Ag@[S−Cu_{56}]. (f) Helical packing in single crystals of PP-Ag@[S−Cu_{56}] and HB-Ag@[S−Cu_{56}]. (g) Experimental geometries (Cu, orange; S, yellow; Ag, gray) and mirror-symmetry models (blue) for each shell with corresponding calculated rCOM values by using (*S*)-HB-[S−Cu_{56}] and (*S*)-HB-Ag@[S−Cu_{56}] as the representative case.

detected by these two techniques. But interestingly, the comparison of electrochemical behaviors of clusters with/without Ag^+ seems to be able to hint at some versions of the overall oxidation states for copper atoms. Cyclic voltammogram of [S−Cu_{56}] displays a pair of quasi-reversible redox peaks at ca. 0.075 and −0.142 V (vs Ag/AgCl), which can be attributed to the Cu(I)/Cu(II) redox couple (Supporting Information, Figure S7).[55,56] This pair of redox peaks becomes significantly diminished in Ag@[S−Cu_{56}], implying that electron transfer might be hindered due to the reduction of the Cu (Supporting Information, Figure S7).

Atomic Structure Retention upon Guest Cation Migration

A more detailed structure anatomy for the two chiral pairs of Ag@[S−Cu_{56}] clusters can be achieved through X-ray single crystal diffraction. It reveals that the two pairs of enantiomeric clusters are structurally analogous, with the respective chemical formulas $Ag@Cu_{56}S_{12}(S^tBu)_{20}(PP)_{12}$ and $Ag@Cu_{56}S_{12}(S^tBu)_{20}(HB)_{12}$. Notably, each pair crystallizes in a space group different from that of their parent clusters (*F*432) (Supporting Information, Figure S9) suggesting the change of intermolecular interactions. Specifically, PP-Ag@[S−Cu_{56}] adopts the *R*3 space group, while HB-Ag@[S−Cu_{56}] crystallizes in $P2_1$. This means the symmetry elements governing molecular packing change. For example, in the parent clusters PP-[S−Cu_{56}] and HB-[S−Cu_{56}], 2-, 3-, and 4-fold rotational axis is present within individual molecules (Supporting Information, Figure S9). In contrast, PP-Ag@[S−Cu_{56}] retains only a 3-fold rotational axis, whereas HB-Ag@[S−Cu_{56}] contains no internal symmetry elements, and the only 2_1-screw axis is located between molecules. Consistent with their chiral space groups, the enantiomeric PP-Ag@[S−Cu_{56}] clusters form clockwise (*R*) or counterclockwise (*S*) helices along the 3_1-screw axis, while the HB-Ag@[S−Cu_{56}] clusters pack helically along the 2_1-screw axis (Figure 3f). Structure solution/refinement unequivocally confirms the presence of a single Ag atom located at the geometric center of these clusters, while the structures of the parent frameworks

https://doi.org/10.1021/jacs.6c03831
J. Am. Chem. Soc. XXXX, XXX, XXX−XXX

remain unchanged (Figure 3b,f). We have carefully inspected the Fourier electron density maps to further rule out the existence of any possible counterions or other species, supporting that all the Ag-containing clusters are intrinsically neutral. This indicates that when a single Ag^+ ion migrates into the center of the cluster, the parent frameworks have been spontaneously reduced by acquiring one additional electron. Such a behavior is unusual in cluster chemistry because it requires the [Cu−S] framework to accept and stably delocalize an extra electron like sp^2-hybrid carbons. By contrast, redox-driven central doping in previously reported systems almost always triggers detectable structural changes, even when subtle, such as ligand or counterion additions.[11,31,38]

To understand the influence of a single core atom on the entire cluster assembly, we must assess how the incorporation of a single Ag atom alters the atomic arrangement of each shell. Single-crystal X-ray diffraction reveals that, relative to their parent clusters, the incorporation of a single Ag atom induces more pronounced structural changes in the inner components than in the outer shell. In both enantiomeric pairs, Ag insertion leads to a similar effect; it results in a less distorted local structures for the $[Cu_{14}]$ dodecahedron, whereas the outer framework remains largely preserved. For example, comparison of (*R*)-PP-$[S{-}Cu_{56}]$ and (*R*)-PP-Ag@$[S{-}Cu_{56}]$ reveals a narrowing of the Cu···Cu distance distribution within the $[Cu_{14}]$ core, evolving from a broad range of 2.44−2.88 Å to a confined window of 2.64−2.71 Å (Supporting Information, Figures S10, S11 and Table S5). A similar trend is observed for the Cu−S bond lengths within the $[Cu_{14}S_{12}]$ framework: upon Ag^+ insertion, the distribution contracts from 1.94−2.55 Å to 2.15−2.33 Å (Supporting Information, Figure S12) due to the increasingly ordered $[Cu_{14}]$ core within the rigid $[S_{12}]$ framework. This enhanced structural regularity can be directly visualized by overlaying the $[Cu_{14}]$ units before and after Ag migration (Supporting Information, Figure S10). The ordering tendency may be attributed to the emerged Ag···Cu interactions. Of note, Ag···Cu distances range from 2.794(4) to 3.034(4) Å (average: 2.893 Å; Supporting Information, Table S5), which are significantly longer than the typical Ag(0)···Cu(0) distance (<2.80 Å), but consistent with the reported Ag(I)···Cu(I) interaction involving the $d^{10}{-}d^{10}$ metallophilic attraction.[47,57,58] This observation is in good agreement with the monovalent oxidation state for the incorporated Ag atom, which aligns well with the XPS results. Despite this enhanced structural rigidity, the average distances for the rest of Cu···Cu remain essentially unchanged (average: 2.68 Å), suggesting that the $[Cu_{14}]$ cage is sufficiently spacious to accommodate the Ag^+ ion without requiring significant framework expansion or contraction. In addition, the distributions and average values of the Cu−S bond lengths in the surface $[Cu_{42}S_{20}]$ shell, as well as the S···S distances within the $[S_{12}]$ and $[S_{20}]$ units, were analyzed and show no obvious differences (Supporting Information, Figures S12, S13 and Table S6). These observations confirm the robustness of the [Cu−S] covalent framework in the present system, which plays a crucial role in maintaining structural integrity throughout the migration process.

Cation Migration-Induced Chiral Perturbation

The migration of Ag^+ cations also influences the chirality (or geometric distortion as it is more general) of the nanocluster framework. Owing to the multishell architecture, the chirality of each shell can be examined independently. To quantify these effects, we performed chiral overlap measurements (COM) for each shell using a modified approach based on the Hausdorff chirality measure.[45,46,59] In this method, an object is optimally superimposed with its mirror image, and the resulting relative COM (rCOM) value quantifies the degree of nonoverlap (see Supporting Information for more information). Consequently, larger rCOM values correspond to greater deviations from mirror symmetry, indicating an enhanced chiral distortion. This investigation shows that Ag^+ incorporation induces comparable chiral modifications across the examined chiral clusters (Supporting Information, Table S7). Taking (*S*)-HB-$[S{-}Cu_{56}]$ and (*S*)-HB-Ag@$[S{-}Cu_{56}]$ as examples (Figure 3g), the rCOM values of the $[S_{12}]$ and $[S_{20}]$ shells show no obvious change and remain below 2%, indicating that the sulfur framework undergoes little structural distortion. A more pronounced variation is observed for the $[Cu_{14}]$ inner-shell. After the Ag^+ incorporation, this dodecahedral core becomes less distorted, as evidenced by a decrease of rCOM values from 5.05% for (*S*)-HB-$[S{-}Cu_{56}]$ to 0.07% for (*S*)-HB-Ag@$[S{-}Cu_{56}]$. In contrast, the rCOM value for the $[Cu_{42}]$ outer shell slightly increases from 14.84% to 18.68%, suggesting a slight increase in the surface distortion. Taken together, these results indicate that Ag^+ incorporation predominantly affects the innermost $[Cu_{14}]$ shell while inducing minor distortions in the outer $[Cu_{42}]$ shell and leaving the sulfide framework essentially intact.

Electronic Structure Investigations

The subtle atomic-level structural perturbations caused by Ag^+ incorporation and reduction of the copper sulfide framework consequently led to observable changes in the electronic structure of the nanoclusters. To elucidate this structure−property correlation, the Ag^+-induced electronic modifications have been analyzed by using a combination of absorption, photoluminescence (PL), circular dichroism (CD), and femtosecond transient absorption (TAS) spectroscopies. Compared with the parent platform $[S{-}Cu_{56}]$, Ag@$[S{-}Cu_{56}]$ ((*R*)-PP-$[S{-}Cu_{56}]$ and (*R*)-PP-Ag@$[S{-}Cu_{56}]$ were used here as the representative examples) shows an 11 nm blueshift of the absorption maximum from 398 to 387 nm, accompanied by a slight broadening of the peak width, while maintaining a similar absorption coefficient (approximately 3.6×10^4, Supporting Information, Figures S15 and S16). In addition, a weak and broad shoulder band centered at ∼570 nm emerges, leading to an overall broadened absorption profile and a darker appearance (Figures 4a and S14). Such changes in the electronic structure originate from modulation of the inorganic core, which have also been observed in other centrally doped metal nanoclusters (e.g., $[Au_{24}(PPh_3)_{10}(PET)_5Cl_2]^+/[Au_{25}(PPh_3)_{10}(PET)_5Cl_2]^{2+}$, $[Ag_{25}(IPBT)_{18}]^-/[AuAg_{24}(IPBT)_{18}]^-$).[11,17] PL analysis reveals that the presence of Ag^+ may also influence their emission behaviors. Upon excitation at 390 nm, both $[S{-}Cu_{56}]$ and Ag@$[S{-}Cu_{56}]$ display a shoulder feature around 415 nm, while their main emission peaks are distinctly separated at 432 nm for Ag@$[S{-}Cu_{56}]$ and 442 nm for $[S{-}Cu_{56}]$ (Supporting Information, Figure S17).

More intriguingly, it demonstrates that the incorporation of a central atom can modulate local chirality attenuation and inversion—without fundamentally altering the overall chiroptical response of the parent clusters (Figures 4b,c and S18). Taking the HB-$[S{-}Cu_{56}]$ → HB-Ag@$[S{-}Cu_{56}]$ transformation as an example, the migration of Ag^+ preserves the overall

https://doi.org/10.1021/jacs.6c03831
J. Am. Chem. Soc. XXXX, XXX, XXX−XXX

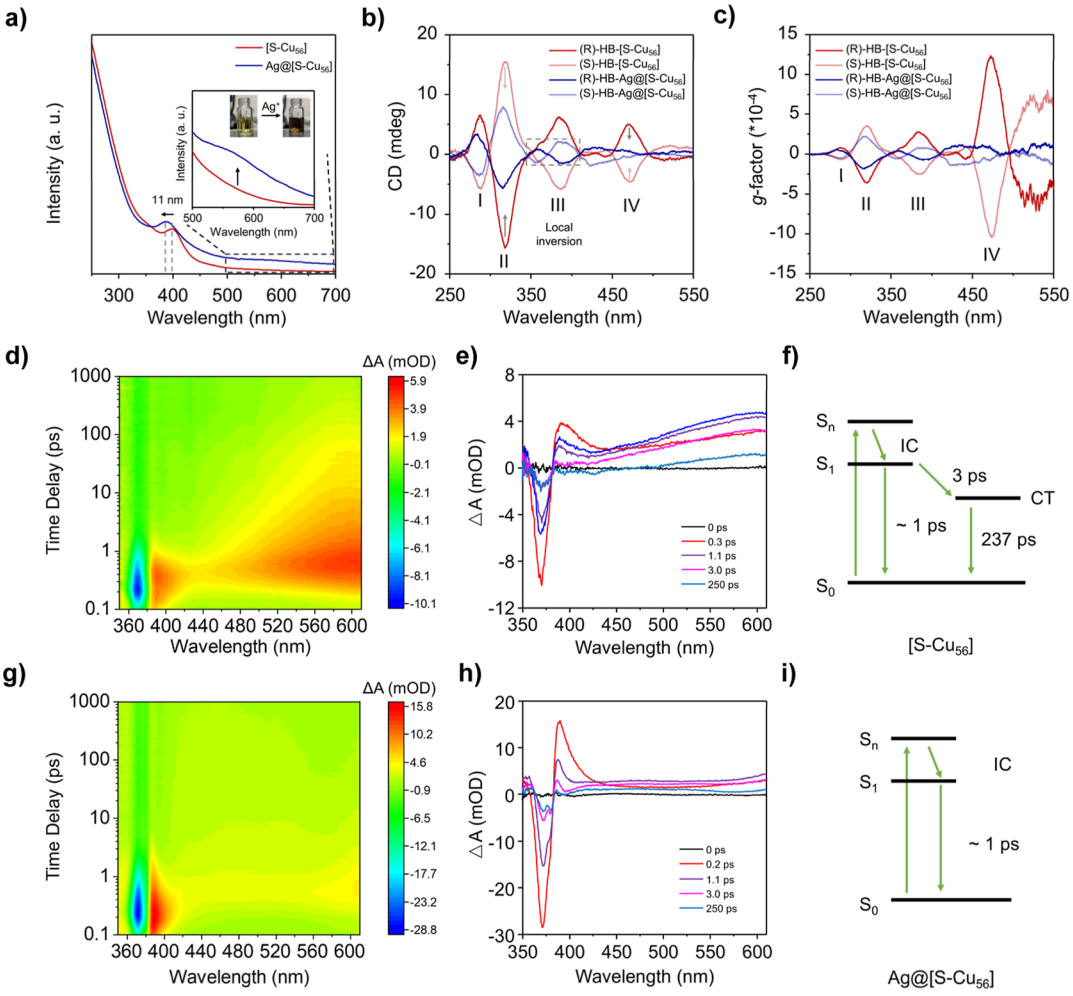

Figure 4. (a) The UV−vis absorption spectra of (*R*)-PP-[S−Cu_{56}]/DCM and (*R*)-PP-Ag@[S−Cu_{56}]/DCM solution (measured at the concentration of 0.2 mg/mL). Inset: enlarged view of the 500−700 nm region. (b) CD spectra of HB-[S−Cu_{56}]/DCM and HB-Ag@[S−Cu_{56}]/DCM solutions measured at the concentration of 0.2 mg/mL. (c) Calculated *g*-factor plots of HB-[S−Cu_{56}]/DCM and HB-Ag@[S−Cu_{56}]/DCM solutions. (d) Contour map of the transient absorption spectra for (*R*)-PP-[S−Cu_{56}]/DCM (pumped at 320 nm). (e) The fs-TA spectra for (*R*)-PP-[S−Cu_{56}]/DCM at different decay times. (f) Relaxation mechanism diagram of (*R*)-PP-[S−Cu_{56}]/DCM. (g) Contour map of the transient absorption spectra for (*R*)-PP-Ag@[S−Cu_{56}]/DCM (pumped at 320 nm). (h) The fs-TA spectra for (*R*)-PP-Ag@[S−Cu_{56}]/DCM at different decay times. (i) Relaxation mechanism diagram of (*R*)-PP-Ag@[S−Cu_{56}].

characteristic CD bands in regions **I** (265 nm−300 nm), **II** (300 nm−345 nm), **III** (345 nm−410 nm), and **IV** (410 nm−495 nm). However, a pronounced attenuation in signal intensities is observed across all bands, most notably in bands **II** and **IV**. Their intensities decrease from approximately 15.5 and 5.0 mdeg to 7.8 and 0.5 mdeg, for bands **II** and **IV**, respectively (Figure 4b). This attenuation can likely be attributed to the isotropic interaction between the inserted Ag^+ and the 14 surrounding Cu atoms of the innermost dodecahedron cage, which diminish the geometric distortion and thereby reduce the overall chiral strength. More interestingly, a local CD inversion is observed in region **III**, manifested as a bisignate Cotton effect with a positive CD signal at 357 nm and a negative CD signal at 390 nm for (*R*)-HB-Ag@[S−Cu_{56}], and the opposite conversion for their enantiomeric counterparts (Figure 4b).[45,60] These spectral evolution trends are consistently reflected in the corresponding *g*-factor plots (Figure 4c). This behavior mimics complex, highly sophisticated biomolecules, in which local chiral elements can be selectively modified without perturbing the global chiral pattern, owing to the presence of weak intermolecular interactions, such as hydrogen bonding or van der Waals forces, that render individual chromophores relatively isolated and independently modulated. In fact, this observation contrasts with the prevailing view that nanoclusters behave as continuous, fully integrated entities, in which even the incorporation of a single atom typically leads to substantial electronic restructuring and, consequently, markedly different optical properties (Supporting Information, Table S10).[18,61,62]

To elucidate the effect of Ag^+ migration and reduction within the [Cu−S] framework on photocarrier dynamics, we conducted a femtosecond transient absorption (fs-TA) investigation, using (*R*)-PP-[S−Cu_{56}] and (*R*)-PP-Ag@[S−Cu_{56}] as model systems. In a typical photoexcitation process, the population is promoted from the ground state (S_0) to higher excited singlet states (S_n), rapidly relaxes to S_1 via internal conversion, and subsequently decays back to the ground state through charge transfer (CT), intersystem crossing (ISC), or direct nonradiative relaxation. Pumping with 320 nm laser pulses, the fs-TA spectra of [S−Cu_{56}] reveal a negative ground state bleaching (GSB) signal at 370 nm and two positive excited-state absorption (ESA) signals around 390

https://doi.org/10.1021/jacs.6c03831
J. Am. Chem. Soc. XXXX, XXX, XXX−XXX

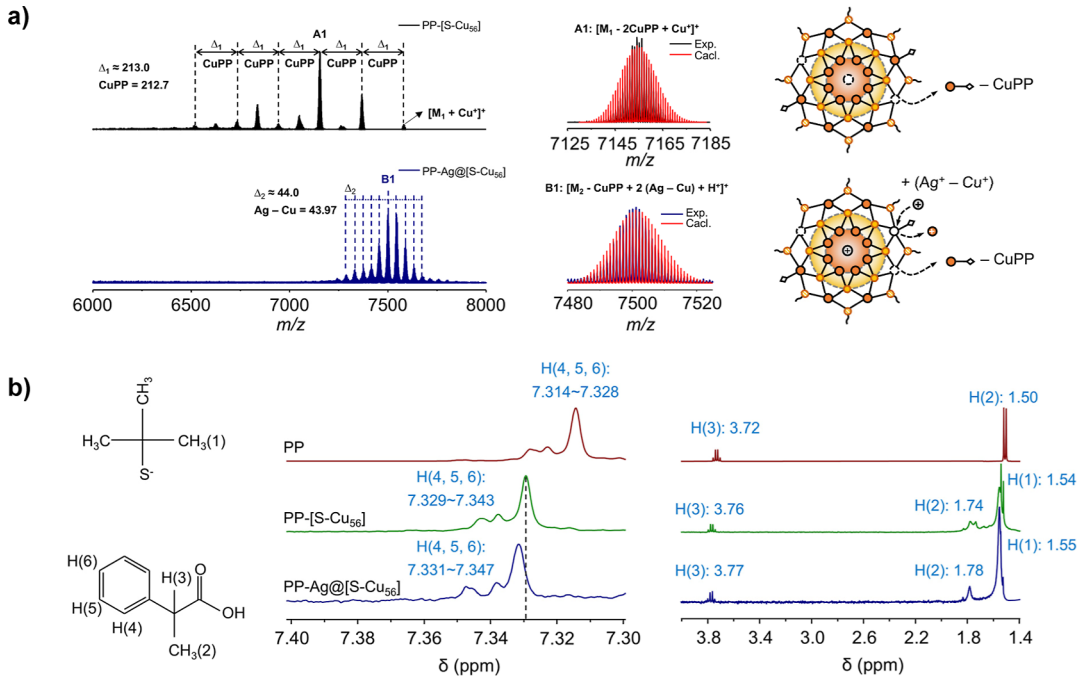

Figure 5. (a) High-resolution ESI-MS spectra of (*R*)-PP-[S−Cu_{56}] and (*R*)-PP-Ag@[S−Cu_{56}] acquired in positive-ion mode, along with the proposed fragmentation pathways. The most intense peak is labeled with the corresponding simulated species. In (*R*)-PP-Ag@[S−Cu_{56}], the spacing between each peak is approximately 44 Da. (b) ^{1}H NMR spectra of (*R*)-PP, (*R*)-PP-[S−Cu_{56}], and (*R*)-PP-Ag@[S−Cu_{56}] recorded in $CDCl_3$. Note: additional ESI-MS spectra and ^{1}H NMR spectra are provided in the Supporting Information (Figures S21−S26).

nm and in the range of 440−610 nm (Figure 4d,e). Kinetic analysis reveals that the decay time of the GSB at 370 nm (∼0.9 ps) closely matches that of the ESA at 390 nm (∼1.1 ps) (Supporting Information, Figure S19), indicating a fast relaxation of the S_1 state back to the ground state, which is commonly observed in metal nanoclusters.[63−67] In contrast, the broad ESA band spanning 440−610 nm exhibits biexponential kinetics, as revealed by biexponential fitting of the kinetic trace at 580 nm, yielding time constants of 3 and 237 ps (Supporting Information, Figure S19). Such long-lived excited states are typically attributed to CT processes, in which photoexcited electrons undergo redistribution of electron density prior to relaxation back to S_0 (Figure 4f).[63,66,67] Upon incorporation of Ag^+, the broad ESA feature in the 440−610 nm region is completely suppressed, whereas the GSB at 370 nm and the ESA at 390 nm remain essentially unchanged (Figure 4g,h). This observation suggests that the excited-state dynamics of Ag@[S−Cu_{56}] are governed by a simpler relaxation pathway, in which the excited electron decays back to the ground state within ∼1 ps (Figures 4i and S20). The suppression of the broad ESA signal in the 440−610 nm range further confirms that this process in [S−Cu_{56}] is associated with CT rather than ISC, since the incorporation of a heavy atom would typically enhance triplet-state formation and strengthen ISC signals.[63−65] This drastic lifetime difference likely arises from electronic quenching owing to the reduction of the [Cu−S] framework, similar to the changes observed in $[Au_{25}(SR)_{18}]^0$ and $[Au_{25}(SR)_{18}]^-$ upon gaining one additional electron.[65]

Comprehensive spectroscopic analyses, including absorption, PL, CD, and TAS, confirm the modulation of electronic structures and excited-state dynamics in the two clusters. In particular, central atom migration induced local chirality inversion, mimicking organic peptide coassemblies that have been explored for sequence-encoded circularly polarized luminescence.[68,69] Together with ready handling of CD intensity through ligand engineering, this enables the current metal sulfide system to serve as a promising platform for wavelength selective chiroptical information storage and encryption, where distinct CD signatures at different wavelengths could serve as orthogonal information channels, analogous to recently demonstrated chiral photonic devices for optical data storage.[70−72]

High-Resolution Mass Spectroscopy, Nuclear Magnetic Resonance, and Electron Paramagnetic Resonance Investigations

The migration of the Ag^+ may also influence the gas-phase behaviors of the title clusters (fragmentation mechanism during the ionization process in the gas phase). Building on our previous investigations of nanoclusters by high-resolution mass spectrometry, we became aware that, unlike noble metal clusters such as Au or Ag, binary semiconductor nanoclusters rarely retain their intact architectures upon ionization, posing significant challenges to elucidating their complete atomic structures.[39,40,50] But interestingly, these semiconductor clusters exhibit distinctive fragmentation behaviors, revealing characteristic gas-phase "signatures" that serve as molecular codes to differentiate clusters of varying composition and structure. In the present work, the incorporation of the Ag^+ ion significantly alters the fragmentation route for this robust copper sulfide nanocluster. The high-resolution electrospray ionization mass spectrometry (ESI-MS) on the parent copper sulfide NC, PP-[S−Cu_{56}] (M_1, M.W. = 7516.96), shows that it has the highest m/z peak at 7580.28 Da (Figure 5a), which can be reasonably attributed to the abduction of a Cu^+ ion on the neutral PP-[S−Cu_{56}] ($[M_1 + Cu^+]^+$) (Supporting Information, Figure S21 and Table S11). The monovalent copper ions likely originate from the complete decomposition of the copper

https://doi.org/10.1021/jacs.6c03831
J. Am. Chem. Soc. XXXX, XXX, XXX−XXX

nanocluster or from the detachment of the surface Cu^+ ion upon impact with source ion during ionization, a phenomenon also reported in related studies.[73] The $[M_1 + Cu^+]^+$ species then undergoes successive fragmentation through the stepwise loss of up to five neutral CuPP units (theoretical mass = 212.71 Da per CuPP unit (Figure 5a)), ultimately yielding a series of evenly spaced ion peaks separated by approximately 213 Da within the 6500−8000 Da range. It is worth noting that continued loss of CuPP units progressively destabilizes the cluster ions; once the number of detached CuPP units exceeds five, the nanocluster undergoes complete structural decomposition, producing low-mass fragments that no longer convey meaningful structural information (Supporting Information, Figure S21). With the presence of the central Ag ion, the PP-Ag@[S−Cu_{56}] (M_2, M.W. = 7624.83) exhibits a quite different fragmentation signature. Though it can also lose one or two neutral CuPP species, its early stage fragmentation mainly involves an interesting cation exchange process. For instance, in the mass range of 7200−7800 Da, several groups of evenly spaced peaks with intervals of approximately 44 Da are observed (Figure 5a). This mass difference precisely corresponds to the substitution of Cu^+ by Ag^+ (**ΔM= 43.97 Da**; Supporting Information, Figure S22 and Table S12). As has been discussed, the Ag^+ ions might be resulted from the complete decomposition of the parent cluster, which again serves as the source ion to interact with the intact PP-Ag@[S−Cu_{56}].

^{1}H NMR investigations were performed on both the neutral organic molecules and the as-prepared nanoclusters, with all protons numbered for clarity (Figures 5b and S23 and S24). Here, we take PP and its corresponding nanocluster derivatives as representative examples to elucidate the changes in the proton chemical environments upon Ag^+ incorporation. Both [S−Cu_{56}] and Ag@[S−Cu_{56}] can be designated by their coordinated organic ligands, $(S^tBu)^-$ and PP, on their surfaces ((*R*)-PP-[S−Cu_{56}] and (*R*)-PP-Ag@[S−Cu_{56}] were used here as the representative examples). As a neutral molecule, HS^tBu exhibits two characteristic ^{1}H singlets at 1.28 and 1.69 ppm, with an integration ratio of 1:9.1, corresponding to the −S*H* proton and the three $-C(CH_3)_3$ groups, respectively. $[CuS^tBu]_\infty$ displays a singlet at 1.61 ppm that can be attributed to the H(1) on its thiolate ligand (Supporting Information, Figure S23). The carboxylic acid ligand PP contains six distinct types of protons in addition to the proton on the −COO*H* group. Three adjacent peaks at 7.314−7.328 ppm can be assigned to H(4, 5, and 6) on the benzene ring owing to the deshielding effect induced by its conjugated π-system. The quartet at 3.72 ppm originates from H(3), arising from its coupling with the neighboring $-CH_3$(2) group, observed as a doublet at 1.50 ppm (Figure 5b). In addition, peak integration reveals that the area ratio for H(3):H(2):H(4, 5, 6) is 1:3.0:5.1, which is in line with the molecule structure (Supporting Information, Figure S24). Compared with the neutral ligands, the nanoclusters exhibit an obvious overall downfield shift in their ^{1}H NMR signals, with a further slight downfield shift upon Ag incorporation. In particular, the H(4, 5, 6) signals appear at 7.329−7.343 ppm for [S−Cu_{56}] and shifted to 7.331−7.347 ppm for Ag@[S−Cu_{56}]. Meanwhile, H(1) and H(2), originating from methyl groups in different chemical environments, resonate at 1.54 and 1.74 ppm in [S−Cu_{56}] and shift slightly to 1.55 and 1.78 ppm in Ag@[S−Cu_{56}], respectively. The quartet corresponding to H(3) is located at 3.76 ppm for [S−Cu_{56}] and 3.77 ppm for Ag@[S−Cu_{56}]. In addition, peak integration reveals area ratios of H(3):H(2):H(4, 5, 6):H(1) = 1:3.6:4.0:14.1 and 1:3.6:4.5:15.4 for [S−Cu_{56}] and Ag@[S−Cu_{56}], respectively, which are consistent with their single-crystal structures (theo. = 1:3:5:15, Supporting Information, Figure S24). These shifts suggest that the cluster acquires a single additional electron, which becomes delocalized over the entire [Cu−S] framework. This redistribution of electron density consequently changes the local electronic environments, leading to the observed changes in the NMR signals.

In addition, the ^{1}H NMR spectrum of the raw reaction mother liquor clarifies the involvement of the reducing agent in this redox-driven process. Compared with the purified nanoclusters, the ^{1}H NMR spectrum of the mother liquor reveals several additional resonances in the range of 1.24−1.39 ppm (Supporting Information, Figure S25). These signals can be assigned to organic disulfides (*R*−*S*−*S*−*R*) or thioethers (*R*−*S*−*R*) (Supporting Information, Figure S26), which are typically generated through oxidation of thiolate species. Therefore, the organic thiolate is identified as the species responsible for lowering the oxidation state of copper, as supported by the detection of its corresponding oxidation products.

Solid-state EPR spectra of [S−Cu_{56}] and Ag@[S−Cu_{56}] display different broad resonance signals but share a similar *g* value of approximately 2.09, suggesting that the dominant spin-bearing state is associated with the Cu−S framework rather than being localized on the encapsulated Ag atom (Supporting Information, Figure S27). Importantly, the broad line width and the absence of resolved Cu or Ag hyperfine splitting argue against a simple assignment to isolated Cu(II) centers. Instead, the signal is more consistent with a delocalized [Cu−S]-based spin state, possibly arising from valence-mixed Cu sites. Compared with [S−Cu_{56}], Ag@[S−Cu_{56}] shows an apparently stronger and slightly modified EPR response, implying that the central Ag atom perturbs the electronic structure of the Cu−S framework and changes the delocalization behavior of the spin-bearing states. Therefore, Ag incorporation does not generate a fundamentally new EPR-active center, but electronically modulates the Cu−S framework.

In/Ex Situ Kinetic Monitoring to Elucidate the Migration Mechanism

To understand the migration mechanism at the atomic-level precision, the following key issues should be clarified or considered: (1) confirming that the parent framework undergoes localized structural rearrangements rather than a fragmentation-reconstruction process and (2) establishing an appropriate technique capable of dynamically monitoring structural evolution during the migration process, so as to reveal the migration pathway of the guest metal cation.

In situ optical spectroscopy, including absorption and CD measurements, unambiguously demonstrates that Ag^+ migration into the parent [S−Cu_{56}] proceeds as a continuous process, thereby excluding a fragmentation-reconstruction mechanism. Taking the HB-[S−Cu_{56}] as an example, the characteristic absorption band at 398 nm does not disappear upon addition of AgS^tBu; instead, it gradually blue-shifts to 387 nm over 1 h (Figure 6a), indicating preservation of the cluster framework during Ag^+ incorporation. Consistent with this observation, in situ CD spectra retain the characteristic four-band pattern throughout the reaction while undergoing continuous and traceable spectral evolution. Specifically, the

https://doi.org/10.1021/jacs.6c03831
J. Am. Chem. Soc. XXXX, XXX, XXX−XXX

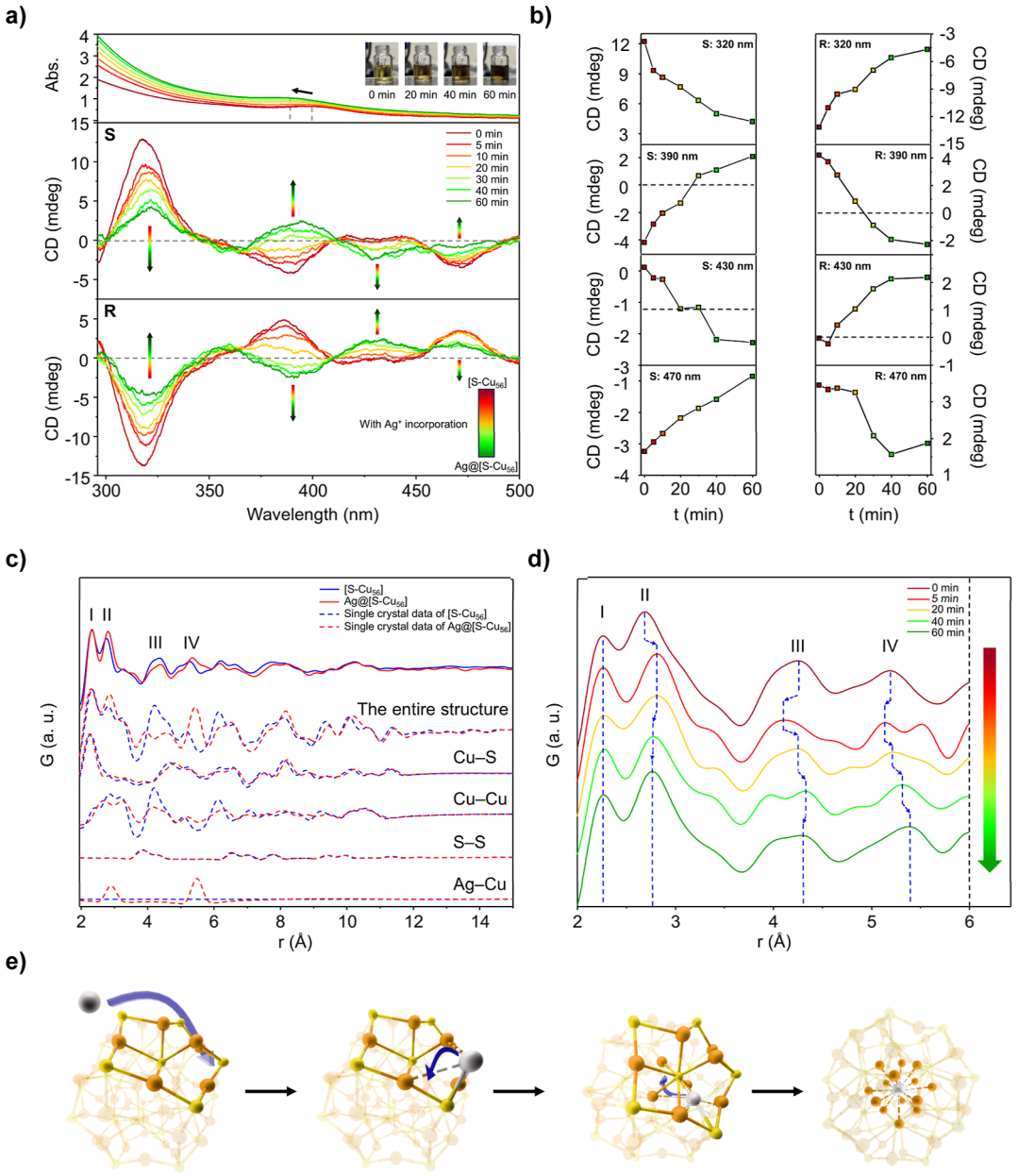

Figure 6. (a) In situ UV−vis and CD spectra monitoring of the Ag^+ migration process from HB-[S−Cu_{56}] to HB-Ag@[S−Cu_{56}]. Inset: snapshots of the solution at different reaction times. (b) Time-dependent evolution of CD signal intensities at 320, 390, 430, and 470 nm during the migration process. (c) Pair distribution function (PDF) analysis of bulk crystalline (*S*)-HB-[S−Cu_{56}] and (*S*)-HB-Ag@[S−Cu_{56}] clusters. The experimental plots for the two clusters are compared with those simulated from single crystal data. (d) Ex situ PDF analysis tracking local structure evolution during the Ag^+ migration process into (*S*)-HB-[S−Cu_{56}]. Full spectra are provided in the Supporting Information (Figure S28). (e) Proposed pathway for Ag^+ migration.

CD intensities at 320 and 470 nm progressively decrease, the 390 nm band undergoes a sign inversion, and a new CD feature at 430 nm emerges over time (Figure 6a,b), collectively supporting a stepwise Ag^+ migration process, rather than a pathway of cluster dissociation and reassembly.

Benefiting from the well-controlled reaction kinetics, ex situ pair distribution function (PDF) analysis allows local structural evolution to be directly traced through systematic changes in characteristic atomic pair distances.[74−76] To establish a difference between the initial and final states of the reaction, PDF measurements were first carried out on the polycrystalline [S−Cu_{56}] and Ag@[S−Cu_{56}] ((*S*)-HB-[S−Cu_{56}] and (*S*)-HB-Ag@[S−Cu_{56}] were used as examples). For both clusters, the PDF profiles display distinct features extending to 11 Å, consistent with nanocluster diameters of ∼1.1 nm. Moreover, the experimental PDFs satisfactorily match those simulated from the single crystal X-ray diffraction data, confirming the structural consistency between the bulk crystalline sample and single crystals (Figure 6c). To better elucidate atomic-level structural changes upon Ag^+ incorporation, we focused on four characteristic PDF signatures (indexed as regions **I**−**IV**, Figure 6c). The features in region **I** remain unchanged for both [S−Cu_{56}] and Ag@[S−Cu_{56}], which corresponding to atomic pair distances of ∼2.32 Å, agreeing well with the covalent Cu−S bond lengths observed in the single crystal structures of [S−Cu_{56}] (average 2.32 Å) and Ag@[S−Cu_{56}] (average 2.31 Å).

https://doi.org/10.1021/jacs.6c03831
J. Am. Chem. Soc. XXXX, XXX, XXX−XXX

This distance arises from a combination of two distinct Cu−S environments: (i) Cu−S bonds in which the $[S_{12}]$ shell bridges the inner $[Cu_{14}]$ cage and the outer $[Cu_{42}]$ shell, and (ii) Cu−S bonds linking the outer $[Cu_{42}]$ shell to the $[S_{20}]$ shell where all S atoms are from surfactant thiolate ligands (Supporting Information, Figure S29). The signal in region **III** likewise exhibits no discernible changes, corresponding to atomic pair distances centered at approximately 4.38 Å. At this separation, no covalent bonding interactions are present; instead, the feature originates from a combination of various interatomic distance correlations, including longer-range Cu···Cu separations such as face-diagonal distances within the $[Cu_{14}]$ unit (average 4.25 Å, Supporting Information, Figure S30) as well as S···S separations within the $[S_{20}]$ shell (average 4.33 Å, Supporting Information, Figure S30). In contrast, the incorporation of a central Ag^+ ion exhibits significant impacts on regions **II** and **IV**. For $[S{-}Cu_{56}]$, a peak at 2.76 Å appears in region **II**, reflecting the averaged Cu···Cu distance within the inner $[Cu_{14}]$ core. Upon Ag^+ incorporation, this peak shifts to 2.81 Å, accompanied by an increased relative intensity and slight broadening (Supporting Information, Figure S32). According to single-crystal structural analysis, this shift originates from the newly formed Ag···Cu interactions (2.94 Å) within the $Ag@[Cu_{14}]$ unit (Supporting Information, Figure S31). Similarly, the atomic separation between the central Ag atom and Cu atoms on the outer $[Cu_{42}S_{20}]$ shell (average 5.45 Å, Supporting Information Figure S31) leads a peak shift from 5.27 Å to 5.35 Å in region **IV**.

Moreover, ex situ PDF analysis of the reaction intermediates reveals a continuous structural transformation, consistent with previous in situ optical spectroscopy observations. The characteristic PDF signal range of the local structure remains constant from 2 to 11 Å throughout the process (Supporting Information, Figure S28), precluding cluster disassembly or reassembly. Furthermore, the evolution of the PDF profiles in regions **I**−**IV** (Figures 6d and S32) supports a dynamic process in which the local framework undergoes subtle yet discernible rearrangements before converging to the final Ag-centered nanocluster through several key steps:

(i) The Ag^+ ion initially adsorbs onto the surface of the $[S{-}Cu_{56}]$, (Figures 6e and S33) driven by its soft-acid affinity toward the surface thiolate ligands,[77] leading to the formation of Ag−S bonds and Ag···Cu interactions. This process is evidenced by the broadening of the peak in region **I**, arising from the longer covalent Ag−S bonds relative to the parent Cu−S bonds.[78] In addition, a peak shift in region **II** from 2.69 to 2.81 Å is observed after 5 min, which is attributed to the formation of longer Ag···Cu interactions compared with Cu···Cu separations.[47]

(ii) Then, Ag^+ may migrate into the interstitial space between the $[S_{12}]$ and $[Cu_{42}S_{20}]$ shells, forming a metastable intermediate that may involve linear S−Ag−S coordination, which is known to be a favorable motif for Ag^+ species (Figures 6e and S33).[79] This behavior is suggested by the formation of additional Ag−S bonds and Ag···Cu interactions, as inferred from the increasing peak widths in region **I** and **II** between 5 and 20 min (Supporting Information, Figure S32).

(iii) Ultimately, Ag^+ occupies the cluster center, interacting with the surrounding 14 Cu atoms to reach the thermodynamically stable state (Figure 6e). After 20 min, the peak width in region **I** gradually returns to that of the parent nanocluster, (Supporting Information, Figure S32) indicating the recovery of the [Cu−S] framework and cleavage of transient Ag−S bonds. And the peak in region **II** continuously shifts toward shorter distances and converges at 2.77 Å, suggesting the establishment of stronger Ag···Cu interactions. During the above process, the features in regions **III** and **IV** exhibit complex evolution and ultimately settle at the characteristic signals of pure $Ag@[S{-}Cu_{56}]$, suggesting a transient distortion and subsequent restoration of the inorganic component. These observations indicate that the relatively weak Cu···Cu interactions impart a certain degree of mobility to the copper framework,[80−82] thereby facilitating the inward migration of Ag^+.

In short, reduction of the parent [Cu−S] framework creates a charge imbalance, thereby driving the stepwise migration of Ag^+ into the center of the copper sulfide nanocluster. In this process, the rigid Cu−S covalent bonding ensures structural stability without complete fragmentation, whereas the weaker Cu···Cu interactions endow the structure with sufficient flexibility,[82,83] ultimately enabling a unique inorganic framework capable of hosting cations.

CONCLUSIONS

This study demonstrates that atomically precise colloidal nanoclusters can exhibit a level of internal adaptability that is uncommon among those of inorganic nanocrystals. By exploiting a chiral copper sulfide framework with a mixed-valence Cu(II)/Cu(I) configuration, we show that controlled electron uptake can be achieved to drive the inward migration of a single metal cation while preserving the overall structural framework. This represents a strategic advance that combines redox responsiveness with structural stability, enabling a central single-atom occupation to occur within a rigid preformed host rather than through fragmentation or reassembly. It also highlights a means of atomic-level manipulation, in which local structural and chiral features can be modified independently of the global architecture.

Looking forward, the deliberate selection of the central guest atom emerges as a powerful handle for tuning local structure and electronic properties without compromising the host framework. In the present study, Ag^+ serves as one illustrative example; it is envisioned that the synthetic strategy and framework robustness allow for the incorporation of a wide range of guest cations beyond Ag^+, including transition metals (e.g., Au^+, Pd^{2+}) and even lanthanides, simply by varying the metal precursor and adjusting the reduction conditions. This cation tunability provides a direct route to tailor redox potentials, optical absorption, and chiral selectivity. As a result, the chiral nanocluster platform offers potential for various applications, such as enantioselective catalysis (including asymmetric hydrogenation or, with appropriate metal centers, C−C bond formation), chiral sensing of biomolecules, and energy related uses like lithium-ion storage or electrocatalytic CO_2 reduction. Extending this concept to diverse host guest combinations and redox chemistries may establish a broadly applicable platform for nanoscience, enabling programmable nanomaterials with responsive optical, electronic, and catalytic functionalities that bridge molecular level precision with solid state robustness.

https://doi.org/10.1021/jacs.6c03831
J. Am. Chem. Soc. XXXX, XXX, XXX−XXX

■ ASSOCIATED CONTENT

Supporting Information

The Supporting Information is available free of charge at https://pubs.acs.org/doi/10.1021/jacs.6c03831.

> Synthetic details, single crystal X-ray data, X-ray photoelectron spectroscopy, X-ray absorption near-edge spectroscopy, cyclic and differential pulse voltammograms, COM calculations, photoluminescent spectroscopy, circular dichroism spectroscopy, femtosecond transient absorption spectroscopy, nuclear magnetic resonance spectroscopy electron paramagnetic resonance spectroscopy, pair distribution function analysis and electrospray ionization mass spectrometry (PDF)

Accession Codes

Deposition Numbers 2521309−2521316 contain the supplementary crystallographic data for this paper. These data can be obtained free of charge via the joint Cambridge Crystallographic Data Centre (CCDC) and Fachinformationszentrum Karlsruhe Access Structures service.

■ AUTHOR INFORMATION

Corresponding Authors

Long Yang − *Interdisciplinary Materials Research Center, School of Materials Science and Engineering, Tongji University, Shanghai 201804, China;* orcid.org/0000-0001-8731-0172; Email: long_yang@tongji.edu.cn

Zheng Zhou − *Interdisciplinary Materials Research Center, School of Materials Science and Engineering, Tongji University, Shanghai 201804, China;* orcid.org/0000-0001-8905-9663; Email: zhouzheng@tongji.edu.cn

Haixiang Han − *Interdisciplinary Materials Research Center, School of Materials Science and Engineering, Tongji University, Shanghai 201804, China;* orcid.org/0000-0002-8465-9624; Email: hxhan@tongji.edu.cn

Authors

Yuhao Jin − *Interdisciplinary Materials Research Center, School of Materials Science and Engineering, Tongji University, Shanghai 201804, China;* orcid.org/0009-0006-5093-8074

Hao Fang − *Interdisciplinary Materials Research Center, School of Materials Science and Engineering, Tongji University, Shanghai 201804, China*

Haoyu Pan − *Interdisciplinary Materials Research Center, School of Materials Science and Engineering, Tongji University, Shanghai 201804, China*

Zhenyi Zhang − *Bruker (Beijing) Scientific Technology Co. Ltd., Shanghai 200233, China*

Chaofeng Liu − *Interdisciplinary Materials Research Center, School of Materials Science and Engineering, Tongji University, Shanghai 201804, China;* orcid.org/0000-0003-2942-1418

Complete contact information is available at: https://pubs.acs.org/10.1021/jacs.6c03831

Notes

The authors declare no competing financial interest.

■ ACKNOWLEDGMENTS

The authors thank Tianyi Liao (Tongji University) for the discussion on electrochemical tests and Meng Zhou (University of Science and Technology of China) for the discussion on femtosecond transient absorption investigations. This work was supported by the Fundamental Research Funds for the Central Universities, the Instrument Analysis Center of Tongji University, the National Natural Science Foundation of China (22101205, 22301219, 22571236 and 52302193). We thank the staff at SSRF BL17B1 beamline of the National Facility for Protein Science in Shanghai (NFPS), Shanghai Advanced Research Institute, CAS, for providing technical support in X-ray diffraction data collection and analysis. The authors acknowledge the beamline BL12SW (http://cstr.cn/31124.02.SSRF.BL12SW) of Shanghai Synchrotron Radiation Facility (SSRF) in China for the X-ray PDF experiment, which was supported by the SSRF proposal No. 2023-SSRF-PT-504692.

■ REFERENCES

(1) Jiang, J.; Chu, S.; Zhang, Y.; Sun, G.; Jin, J.; Zeng, X.; Chen, M.; Liu, P. Crystal Plane Orientation-Dependent Surface Atom Diffusion in Sub−10-nm Au Nanocrystals. *Sci. Adv.* **2024**, *10*, No. eadn5946.

(2) Son, D.; Hughes, S. M.; Yin, Y.; Paul Alivisatos, A. Cation Exchange Reactions in Ionic Nanocrystals. *Science* **2004**, *306*, 1009−1012.

(3) Norris, D. J.; Efros, A. L.; Erwin, S. C. Doped Nanocrystals. *Science* **2008**, *319*, 1776−1779.

(4) Cargnello, M.; Johnston-Peck, A. C.; Diroll, B. T.; Wong, E.; Datta, B.; Damodhar, D.; Doan-Nguyen, V. V.; Herzing, A. A.; Kagan, C. R.; Murray, C. B. Substitutional Doping in Nanocrystal Superlattices. *Nature* **2015**, *524* (7566), 450−453.

(5) Vlaskin, V. A.; Barrows, C. J.; Erickson, C. S.; Gamelin, D. R. Nanocrystal Diffusion Doping. *J. Am. Chem. Soc.* **2013**, *135* (38), 14380−14389.

(6) Li, B.; Li, X.; Gao, W.; Jiang, Q. An Effective Scheme to Determine Surface Energy and Its Relation with Adsorption Energy. *Acta Mater.* **2021**, *212*, 116895.

(7) Nanda, K. K.; Maisels, A.; Kruis, F. E.; Fissan, H.; Stappert, S. Higher Surface Energy of Free Nanoparticles. *Phys. Rev. Lett.* **2003**, *91* (10), 106102.

(8) Bose, R.; Manna, G.; Pradhan, N. Surface Doping for Hindrance of Crystal Growth and Structural Transformation in Semiconductor Nanocrystals. *J. Phys. Chem. C* **2013**, *117* (40), 20991−20997.

(9) Yao, C.; Lin, Y. J.; Yuan, J.; Liao, L.; Zhu, M.; Weng, L. H.; Yang, J.; Wu, Z. Mono-Cadmium vs Mono-Mercury Doping of Au_{25} Nanoclusters. *J. Am. Chem. Soc.* **2015**, *137* (49), 15350−15353.

(10) Lei, Y.; Butler, D.; Lucking, M. C.; Zhang, F.; Xia, T.; Fujisawa, K.; Granzier-Nakajima, T.; Cruz-Silva, R.; Endo, M.; Terrones, H.; Terrones, M.; Ebrahimi, A. Single-Atom Doping of MoS_2 with Manganese Enables Ultrasensitive Detection of Dopamine: Experimental and Computational Approach. *Sci. Adv.* **2020**, *6*, No. eabc4250.

(11) Wang, S.; Abroshan, H.; Liu, C.; Luo, T.; Zhu, M.; Kim, H. J.; Rosi, N. L.; Jin, R. Shuttling Single Metal Atom into and out of a Metal Nanoparticle. *Nat. Commun.* **2017**, *8* (1), 848.

(12) Xiong, G.; Clark, J. N.; Nicklin, C.; Rawle, J.; Robinson, I. K. Atomic Diffusion within Individual Gold Nanocrystal. *Sci. Rep.* **2014**, *4*, 6765.

(13) White, S. L.; Smith, J. G.; Behl, M.; Jain, P. K. Co-operativity in a Nanocrystalline Solid-State Transition. *Nat. Commun.* **2013**, *4*, 2933.

(14) Ma, F.; Ivanov, S. A.; Dobrzycki, L. M.; Zeng, C. Programmable Synthesis of Atomically Precise Semiconductor Artificial Atoms. *Nat. Synth.* **2025**, *4* (10), 1258−1269.

(15) Robinson, R. D.; Sadtler, B.; Demchenko, D. O.; Erdonmez, C. K.; Wang, L.; Alivisatos, A. P. Spontaneous Superlattice Formation in

Nanorods Through Partial Cation Exchange. *Science* **2007**, *317*, 355−358.
(16) Liu, Y.; Chai, X.; Cai, X.; Chen, M.; Jin, R.; Ding, W.; Zhu, Y. Central Doping of a Foreign Atom into the Silver Cluster for Catalytic Conversion of CO_2 toward C−C Bond Formation. *Angew. Chem., Int. Ed.* **2018**, *57* (31), 9775−9779.
(17) Yoo, S.; Kim, D.; Deng, G.; Chen, Y.; Lee, K.; Yoo, S.; Liu, X.; Tang, Q.; Hwang, Y. J.; Hyeon, T.; Bootharaju, M. S. Impact of Heterocore Atoms on CO_2 Electroreduction in Atomically Precise Silver Nanoclusters. *J. Am. Chem. Soc.* **2025**, *147* (15), 12546−12554.
(18) Ding, X.; Shi, L.; Wang, J.; Xu, L.; Zhang, L.; Chen, Z. Doping Copper(I) in Ag_7 Cluster for Circularly Polarized OLEDs with External Quantum Efficiency of 26.7. *Angew. Chem., Int. Ed.* **2025**, *64* (5), No. e202417934.
(19) Bian, G.; Chen, D.; Chen, Y.; Zhang, W.; Fang, L.; You, Q.; Wang, R.; Gu, W.; Zhou, Y.; Yan, N.; Zhuang, S.; Ji, S.; Zhou, M.; Wang, C.; Liao, L.; Tang, Q.; Yang, J.; Wu, Z. Remove the Innermost Atom of a Magnetic Multi-Shell Gold Nanoparticle for Near-Unity Conversion of CO_2 to CO. *Sci. Adv.* **2025**, *11*, No. eadu1996.
(20) Takano, S.; Hirai, H.; Nakashima, T.; Iwasa, T.; Taketsugu, T.; Tsukuda, T. Photoluminescence of Doped Superatoms $M@Au_{12}$ (M = Ru, Rh, Ir) Homoleptically Capped by $(Ph_2)PCH_2P(Ph_2)$: Efficient Room-Temperature Phosphorescence from $Ru@Au_{12}$. *J. Am. Chem. Soc.* **2021**, *143* (28), 10560−10564.
(21) Yang, H.; Peng, S.; Chen, W.; Luo, D.; Xi, S.; Lu, S.; Huang, Y.; Hao, D.; Cai, B.; Wang, H.; Xie, M.; Li, M.; Li, X.; Ning, G.; Li, D. Double-Helical Assembly of a Copper-Silver Hydride Cluster Exhibiting Thermally Activated Delayed Fluorescence. *CCS Chem.* **2025**, *7* (7), 2201−2214.
(22) Goicoechea, J. M.; Sevov, S. C. Deltahedral Germanium Clusters: Insertion of Transition-Metal Atoms and Addition of Organometallic Fragments. *J. Am. Chem. Soc.* **2006**, *128*, 4155−4161.
(23) Tellgmann, R.; Krawez, N.; Lin, S. H.; Hertel, I. V.; Campbell, E. E. B. Endohedral Fullerene Production. *Nature* **1996**, *382*, 407−408.
(24) Peng, R.; Chu, S.; Huang, Y.; Yu, H.; Wang, T.; Jin, B.; Fu, Y.; Wang, C. Preparation of $He@C_{60}$ and $He_2@C_{60}$ by an Explosive Method. *J. Mater. Chem.* **2009**, *19* (22), 3602−3605.
(25) Rubin, Y. Organic Approaches to Endohedral Metallofullerenes: Cracking Open or Zipping Up Carbon Shells? *Chem.—Eur. J.* **1997**, *3* (7), 1009−1016.
(26) Komatsu, K.; Murata, M.; Murata, Y. Encapsulation of Molecular Hydrogen in Fullerene C_{60} by Organic Synthesis. *Science* **2005**, *307*, 238−240.
(27) Saunders, M.; Cross, R. J.; Jimenez-Vazquez, H. A.; Shimshi, R.; Khong, A. Noble Gas Atoms inside Fullerenes. *Science* **1996**, *271*, 1693−1697.
(28) Krachmalnicoff, A.; Levitt, M. H.; Whitby, R. J. An Optimised Scalable Synthesis of $H_2O@C_{60}$ and a New Synthesis of $H_2@C_{60}$. *Chem. Commun.* **2014**, *50*, 13037−13040.
(29) Yao, Y.; Shi, X.; Zheng, S.; Chen, Z.; Xie, S.; Huang, R.; Zheng, L. Atomically Precise Insights into Metal−Metal Bonds Using Comparable Endo-Units of Sc_2 and Sc_2C_2. *CCS Chem.* **2021**, *3* (12), 294−302.
(30) Bootharaju, M. S.; Joshi, C. P.; Parida, M. R.; Mohammed, O. F.; Bakr, O. M. Templated Atom-Precise Galvanic Synthesis and Structure Elucidation of a $[Ag_{24}Au(SR)_{18}]^-$ Nanocluster. *Angew. Chem., Int. Ed.* **2016**, *55* (3), 922−926.
(31) Wang, S.; Song, Y.; Jin, S.; Liu, X.; Zhang, J.; Pei, Y.; Meng, X.; Chen, M.; Li, P.; Zhu, M. Metal Exchange Method Using Au_{25} Nanoclusters as Templates for Alloy Nanoclusters with Atomic Precision. *J. Am. Chem. Soc.* **2015**, *137* (12), 4018−4021.
(32) Bootharaju, M. S.; Sinatra, L.; Bakr, O. M. Distinct Metal-Exchange Pathways of Doped Ag_{25} Nanoclusters. *Nanoscale* **2016**, *8* (39), 17333−17339.
(33) van der Linden, M.; van Bunningen, A. J.; Amidani, L.; Bransen, M.; Elnaggar, H.; Glatzel, P.; Meijerink, A.; de Groot, F. M. F. Single Au Atom Doping of Silver Nanoclusters. *ACS Nano* **2018**, *12* (12), 12751−12760.
(34) Zheng, K.; Fung, V.; Yuan, X.; Jiang, D.; Xie, J. Real Time Monitoring of the Dynamic Intracluster Diffusion of Single Gold Atoms into Silver Nanoclusters. *J. Am. Chem. Soc.* **2019**, *141* (48), 18977−18983.
(35) Kim, M.; Weerawardene, K. L. D. M.; Choi, W.; Han, S. M.; Paik, J.; Kim, Y.; Choi, M.; Aikens, C. M.; Lee, D. Insights into the Metal-Exchange Synthesis of $MAg_{24}(SR)_{18}$ (M = Ni, Pd, Pt) Nanoclusters. *Chem. Mater.* **2020**, *32* (23), 10216−10226.
(36) Guo, Y.; Torchon, H. S.; Zhu, Y.; Wei, Z.; Zhang, Z.; Han, H.; Petrukhina, M. A.; Zhou, Z. Stepwise Deprotonation of Truxene: Structures, Metal Complexation, and Charge-Dependent Optical Properties. *Chem. Sci.* **2023**, *14* (45), 13219−13227.
(37) Prather, K. V.; Stoffel, J. T.; Tsui, E. Y. Redox Reactions at Colloidal Semiconductor Nanocrystal Surfaces. *Chem. Mater.* **2023**, *35* (9), 3386−3403.
(38) Wu, T.; Zhang, Q.; Hou, Y.; Wang, L.; Mao, C.; Zheng, S.; Bu, X.; Feng, P. Monocopper Doping in Cd−In−S Supertetrahedral Nanocluster via Two-Step Strategy and Enhanced Photoelectric Response. *J. Am. Chem. Soc.* **2013**, *135* (28), 10250−10253.
(39) Fang, H.; Geng, L.; Zhou, Z.; Han, H. A Semiconductor Nanocluster Platform with Four Structural Configurations: An Ionic Pair with Tunable Chirality. *J. Am. Chem. Soc.* **2025**, *147* (34), 31417−31428.
(40) Xu, C.; Zhang, Z.; Zhou, Z.; Han, H. A Chiral CdS Magic-Size Cluster with Enantiomerically-Biased Crystallization. *J. Am. Chem. Soc.* **2025**, *147* (21), 17890−17901.
(41) Luo, X.; Gong, C.; Pan, F.; Si, Y.; Yuan, J.; Asad, M.; Dong, X.; Zang, S.; Mak, T. C. W. Small Symmetry-Breaking Triggering Large Chiroptical Responses of Ag_{70} Nanoclusters. *Nat. Commun.* **2022**, *13* (1), 1177.
(42) Kuznetsova, V. A.; Mates-Torres, E.; Prochukhan, N.; Marcastel, M.; Purcell-Milton, F.; O'Brien, J.; Visheratina, A. K.; Martinez-Carmona, M.; Gromova, Y.; Garcia-Melchor, M.; Gun'ko, Y. K. Effect of Chiral Ligand Concentration and Binding Mode on Chiroptical Activity of CdSe/CdS Quantum Dots. *ACS Nano* **2019**, *13* (11), 13560−13572.
(43) Ma, W.; Xu, L.; de Moura, A. F.; Wu, X.; Kuang, H.; Xu, C.; Kotov, N. A. Chiral Inorganic Nanostructures. *Chem. Rev.* **2017**, *117* (12), 8041−8093.
(44) Bai, M.; Qin, L.; Zeng, X. M.; Wu, M.; Yao, L. Y.; Yang, G. Y. Dithiocarbonate-Protected Au_{25} Nanorods of a Chiral D_5 Configuration and NIR-II Phosphorescence. *J. Am. Chem. Soc.* **2024**, *146* (18), 12734−12742.
(45) Yeom, J.; Santos, U. S.; Chekini, M.; Cha, M.; de Moura, A. F.; Kotov, N. A. Chiromagnetic Nanoparticles and Gels. *Science* **2018**, *359*, 309−314.
(46) Cha, M.; Ma, J.; Kim, J. Y.; Emre, E. S. T.; Kotov, N. A. Graph-Theoretical Chirality Measure and Chirality-Property Relations for Chemical Structures with Multiscale Mirror Asymmetries. *Chirality* **2024**, *36* (6), No. e23678.
(47) Tang, L.; Dong, W.; Han, Q.; Wang, B.; Wu, Z.; Wang, S. Structure and Optical Properties of an $Ag_{135}Cu_{60}$ Nanocluster Incorporating an Ag_{135} Buckminsterfullerene-Like Topology. *Nat. Synth.* **2025**, *4* (4), 506−513.
(48) Chen, Z.; Walsh, A. G.; Wei, X.; Zhu, M.; Zhang, P. Site-Specific Electronic Properties of $[Ag_{25}(SR)_{18}]^-$ Nanoclusters by X-ray Spectroscopy. *Small* **2021**, *17* (27), No. e2005162.
(49) Xu, C.; Jin, Y.; Fang, H.; Zheng, H.; Carozza, J. C.; Pan, Y.; Wei, P.; Zhang, Z.; Wei, Z.; Zhou, Z.; Han, H. A High-Nuclearity Copper Sulfide Nanocluster [S-Cu_{50}] Featuring a Double-Shell Structure Configuration with Cu(II)/Cu(I) Valences. *J. Am. Chem. Soc.* **2023**, *145* (47), 25673−25685.
(50) Jin, Y.; Zhang, Z.; Zheng, H.; Cheng, X.; Geng, L.; Zhou, Z.; Han, H. Unveiling the Formation Mechanism for Binary Semiconductor Nanoclusters: A Two-Step Pathway to a Double-Shell Structured Copper Sulfide Nanocluster. *ACS Nano* **2024**, *18* (49), 33681−33695.

https://doi.org/10.1021/jacs.6c03831
J. Am. Chem. Soc. XXXX, XXX, XXX−XXX

(51) Wang, Y.; Im, J.; Soares, J. W.; Steeves, D. M.; Whitten, J. E. Thiol Adsorption on and Reduction of Copper Oxide Particles and Surfaces. *Langmuir* **2016**, *32* (16), 3848−3857.
(52) Ferraria, A. M.; Carapeto, A. P.; Botelho do Rego, A. M. X-ray Photoelectron Spectroscopy: Silver Salts Revisited. *Vacuum* **2012**, *86* (12), 1988−1991.
(53) Li, C.; Shen, Z.; Hu, Y.; Tang, Y.; Chen, W.; Ren, B. Insights into the Structures and Electronic Properties of Cu_{n+1}^{μ} and Cu_nS^{μ} (n = 1−12; μ = 0, ±1) Clusters. *Sci. Rep.* **2017**, *7* (1), 1345.
(54) Li, M.; Wang, Z.; Yang, L.; Li, D.; Yao, Q. R.; Rao, G. H.; Gao, X. P. A.; Zhang, Z. Electron Delocalization and Relaxation Behavior in Cu-Doped Bi_2Se_3 Films. *Phys. Rev. B* **2017**, *96* (7), 075152.
(55) Zhang, S.; Zhao, L. A Merged Copper(I/II) Cluster Isolated from Glaser Coupling. *Nat. Commun.* **2019**, *10* (1), 4848.
(56) Cope, J. D.; Valle, H. U.; Hall, R. S.; Riley, K. M.; Goel, E.; Biswas, S.; Hendrich, M. P.; Wipf, D. O.; Stokes, S. L.; Emerson, J. P. Tuning the Copper(II)/Copper(I) Redox Potential for More Robust Copper-Catalyzed C−N Bond Forming Reactions. *Eur. J. Inorg. Chem.* **2020**, *2020*, 1278−1285.
(57) Brocha Silalahi, R. P.; Chiu, T.-H.; Kao, J.-H.; Wu, C.-Y.; Yin, C.-W.; Liu, Y.-C.; Chen, Y. J.; Saillard, J.-Y.; Chiang, M.-H.; Liu, C. W. Synthesis and Luminescence Properties of Two-Electron Bimetallic Cu−Ag and Cu−Au Nanoclusters via Copper Hydride Precursors. *Inorg. Chem.* **2021**, *60* (14), 10799−10807.
(58) Khan, R. A.; Jaafar, M. H.; Hadi, A. D.; Alsaeedi, H.; Alsalme, A. Luminescent Tetranuclear Ag(I)/Cu(I) Cubane Clusters: Investigating Argentophilicity, Cuprophilicity, and Mixed Argento-Cuprophilicity. *Inorg. Chim. Acta* **2025**, *578*, 122517.
(59) Buda, A. B.; Mislow, K. A Hausdorff Chirality Measure. *J. Am. Chem. Soc.* **1992**, *114*, 6006−6012.
(60) Hsu, M.; Woody, R. W. The Origin of the Heme Cotton Effects in Myoglobin and Hemoglobin. *J. Am. Chem. Soc.* **1971**, *93* (14), 3515−3525.
(61) Krishnadas, K. R.; Sementa, L.; Medves, M.; Fortunelli, A.; Stener, M.; Fürstenberg, A.; Longhi, G.; Bürgi, T. Chiral Functionalization of an Atomically Precise Noble Metal Cluster: Insights into the Origin of Chirality and Photoluminescence. *ACS Nano* **2020**, *14* (8), 9687−9700.
(62) Yin, B.; Kong, J.; Guo, M.; Kong, J.; You, Q.; Zhou, M.; Luo, Z. Heterometal Doping Modulates Luminescent and Chiroptical Behavior in Superatomic M_1Ag_{14} (M = Pd, Pt) Clusters. *Small* **2025**, *21* (33), 2504958.
(63) Liu, X.; Zhou, X.; Lei, X.; Kong, J.; Zhang, W.; Zhou, M.; Wang, L.; Xu, W. W.; Zhu, Y. An Unprecedented Two-Dimensional Pattern in Gold Nanoclusters Bred by Interlocking Au_4 Blocks. *J. Am. Chem. Soc.* **2025**, *147* (46), 42758−42765.
(64) Zhao, R.; Zeng, L.; Zhao, F.; Lan, P.; Kang, X.; Zhu, M.; Luo, Y.; Zhou, M. Understanding the NIR Emission of Metal Nanoclusters Through a Ligand-Shell-Kernel Triad Picture. *JACS Au* **2025**, *5* (11), 5470−5480.
(65) Zhou, M.; Yao, C.; Sfeir, M. Y.; Higaki, T.; Wu, Z.; Jin, R. Excited-State Behaviors of $M_1Au_{24}(SR)_{18}$ Nanoclusters: The Number of Valence Electrons Matters. *J. Phys. Chem. C* **2018**, *122* (25), 13435−13442.
(66) Guo, Y.; Zhang, Z.; Han, H.; Zhou, Z. Chiral Separation of Copper Sulfide [S−Cu_{36}] Nanocluster Using a Chiral Adaptive Counterion. *Nano Lett.* **2024**, *24* (38), 11985−11991.
(67) Zhang, W.; Luo, L.; Liu, Z.; Zhao, F.; Kong, J.; Jin, R.; Luo, Y.; Zhou, M. Evolution of Coherent Vibrations in Atomically Precise Gold Quantum Rods with Periodic Elongation. *Sci. Adv.* **2025**, *11*, No. eadx2781.
(68) Li, Q.; Zhang, J.; Wang, Y.; Zhang, G.; Qi, W.; You, S.; Su, R.; He, Z. Self-Assembly of Peptide Hierarchical Helical Arrays with Sequence-Encoded Circularly Polarized Luminescence. *Nano Lett.* **2021**, *21* (15), 6406−6415.
(69) Zhao, J.; Dou, W.-T.; Cui, W.; Shi, X.; Li, X.; Fang, J.; Qian, X.; Yang, H.-B.; Xu, L. Chiroptical Signal Inversion of Peptido-Coassemblies in Confined Parallel-Laminar Microfluidics. *Angew. Chem., Int. Ed.* **2025**, *64* (27), No. e202503284.
(70) Lee, Y. H.; Won, Y.; Mun, J.; Lee, S.; Kim, Y.; Yeom, B.; Dou, L.; Rho, J.; Oh, J. H. Hierarchically Manufactured Chiral Plasmonic Nanostructures with Gigantic Chirality for Polarized Emission and Information Encryption. *Nat. Commun.* **2023**, *14* (1), 7298.
(71) Sha, X.; Du, K.; Zeng, Y.; Lai, F.; Yin, J.; Zhang, H.; Song, B.; Han, J.; Xiao, S.; Kivshar, Y.; Song, Q. Chirality Tuning and Reversing with Resonant Phase-Change Metasurfaces. *Sci. Adv.* **2024**, *10*, No. eadn9017.
(72) Li, E.; Dong, M.; Ding, D.; Shi, B.; Guo, G.; Nori, F. All-Optically Tunable Electromagnetic Chirality Transfer. *Sci. Adv.* **2026**, *12*, No. eadv3124.
(73) Brocha Silalahi, R. P.; Huang, G.-R.; Liao, J.-H.; Chiu, T.-H.; Chakrahari, K. K.; Wang, X.; Cartron, J.; Kahlal, S.; Saillard, J.-Y.; Liu, C. W. Copper Clusters Containing Hydrides in Trigonal Pyramidal Geometry. *Inorg. Chem.* **2020**, *59* (4), 2536−2547.
(74) Egami, T.; Billinge, S. J. L. *Underneath the Bragg Peaks: Structural Analysis of Complex Materials*, 2nd ed.; *Pergamon Materials Series*; Elsevier: Amsterdam, 2012.
(75) Juhás, P.; Davis, T.; Farrow, C. L.; Billinge, S. J. L. PDFgetX3: A Rapid and Highly Automatable Program for Processing Powder Diffraction Data into Total Scattering Pair Distribution Functions. *J. Appl. Crystallogr.* **2013**, *46* (2), 560−566.
(76) Billinge, S. J. L.; Skjaervoe, S. H.; Terban, M. W.; Tao, S.; Yang, L.; Rakita, Y.; Frandsen, B. A. Local Structure Determination Using Total Scattering Data. In *Comprehensive Inorganic Chemistry III*; Elsevier, 2023; pp 222−247.
(77) Pearson, R. G. Hard and Soft Acids and Bases. *J. Am. Chem. Soc.* **1963**, *85*, 3533−3539.
(78) Abramov, P. A.; Sokolov, M. N. Crystal Structure of [Ag(S*t*Bu)]. *J. Struct. Chem.* **2025**, *66* (5), 998−1006.
(79) Joshi, C. P.; Bootharaju, M. S.; Alhilaly, M. J.; Bakr, O. M. $[Ag_{25}(SR)_{18}]^-$: The "Golden" Silver Nanoparticle. *J. Am. Chem. Soc.* **2015**, *137* (36), 11578−11581.
(80) Dong, Y.; Dong, S.; Yu, C.; Liu, J.; Gai, S.; Xie, Y.; Zhao, Z.; Qin, X.; Feng, L.; Yang, P.; Zhao, Y. Mitochondria-Targeting Cu_3VS_4 Nanostructure with High Copper Ionic Mobility for Photothermoelectric Therapy. *Sci. Adv.* **2023**, *9*, No. eadi9980.
(81) Weldert, K. S.; Zeier, W. G.; Day, T. W.; Panthöfer, M.; Snyder, G. J.; Tremel, W. Thermoelectric Transport in Cu_7PSe_6 with High Copper Ionic Mobility. *J. Am. Chem. Soc.* **2014**, *136* (34), 12035−12040.
(82) Mehrotra, P. K.; Hoffmann, R. Cu(I)−Cu(I) Interactions. Bonding Relationships in d^{10}−d^{10} Systems. *Inorg. Chem.* **1978**, *17* (8), 2187−2189.
(83) Sculfort, S.; Braunstein, P. Intramolecular d^{10}−d^{10} Interactions in Heterometallic Clusters of the Transition Metals. *Chem. Soc. Rev.* **2011**, *40* (5), 2741−2760.

https://doi.org/10.1021/jacs.6c03831
J. Am. Chem. Soc. XXXX, XXX, XXX−XXX